

Residual neural networks to classify the high frequency emission in core-collapse supernova gravitational waves

Manuel D. Morales^a, Javier M. Antelis^b, Claudia Moreno^a

^a*Departamento de Física, CUCEI, Universidad de Guadalajara, Guadalajara, 44430, Jalisco, México,*

^b*Escuela de Ingeniería y Ciencias, Tecnológico de Monterrey, Monterrey, 64849, Nuevo León, México,*

Abstract

We present the results of a detailed study on the detectability of the High Frequency Feature (HFF) in core-collapse supernova (CCSN) gravitational wave (GW) signals. We applied Residual Neural Networks (ResNet50), one of the state-of-the-art deep learning architectures in computer vision, to perform a multi-class classification of image samples built from time-frequency Morlet wavelet scalograms of LIGO-Virgo noise plus CCSN GW signals. We consider three target labels for three consecutive and mutually exclusive intervals in which the (first-order) slope of the HFF can be located. We optimized, trained, and tested the ResNet50 model with phenomenological waveforms. Next, we tested the optimized ResNet50 model with GW signals from CCSN simulations. At galactic distances of 1Kpc and 5Kpc with H1 and L1 data and 1Kpc with V1 data, we obtained highly accurate results (test accuracies from 0.8933 to 0.9867), which show the feasibility of our methodology. In the case of further distances, we observed declines in test performance until 0.8000 with H1 and L1 data at 10Kpc and until 0.5933 with V1 data at 10Kpc. Without assuming the continuity and/or discontinuity of the HFF slope values, our methodology is general enough to address, at an early stage, the characterization of the HFF.

Keywords: gravitational waves, Deep Learning, convolutional neural networks, core-collapse supernovae, LIGO-Virgo detectors

Email addresses: manueld.morales@academicos.udg.mx (Manuel D. Morales), mauricio.antelis@tec.mx (Javier M. Antelis), claudia.moreno@academicos.udg.mx (Claudia Moreno)

1. Introduction

Thanks to pioneering detections of gravitational wave signals emitted by binary black holes [1] and binary neutron stars [2], we entered an exciting new era of multi-messenger astronomy [3]. Nowadays, GW signals emitted by compact binary coalescences (CBC) have their standard place in most analyses to detect and estimate parameters in GW signals. Moreover, observational prospects are even wider for considering other kinds of GW signals, such as those emitted by core-collapse supernovae (CCSNe). These signals will be potentially detectable with the current generation of interferometric detectors [4].

CCSNe are extremely violent astrophysical processes. They occur at the end of the lifetime of massive stars with initial masses of $9M_{\odot} \lesssim M \lesssim 25M_{\odot}$, and belonging to a metallicity range from metal-free stars to those with metallicity about the solar [5]. According to the basic overall picture of CCSNe [6], at the end of the life of massive stars with initial masses $M \geq 10M_{\odot}$, an iron core is formed, which in turn, after dissociation of its iron nuclei into alpha particles and free nucleons (due to collisions caused by ultra-energetic photons), undergoes a dynamical collapse. This collapse continues until the falling matter reaches supranuclear densities and a stiff proto-neutron star (PNS) is formed. In addition, as a result of the inner core bounce, a shock wave formed by the outer shells of the stellar envelope, with its own physical mechanism involved in its generation, revival, and propagation, is launched into the interstellar medium.

CCSNe emit GW signals because of the aspherical dynamics occurring in a strong gravity regime. From an inverse problem approach, we expect these signals to carry information about physical processes involved in the explosion, printed as features or signatures. This is also pointed out in the state-of-the-art numerical CCSNe simulations. Then, with this theoretical assumption at hand, the big challenge in CCSNe GW data analysis is to implement new algorithms to detect and estimate the parameters of these features.

Among the physical processes involved in CCSNe, those that occur in the PNS are the ones that contribute the most to the emission of GW signals [5]. By simply exploring the TF representation of simulated CCSN GW signals (such as spectrograms, scalograms, etc.), this feature (usually

called “g-mode”) is present in many of the state-of-the-art simulations (as those studied in [4]) unless it is filtered, as a post hoc procedure, to enhance the presence of other features. It also seems to give significant hints about the evolution of PNS. After the core bounce, this feature has an increasing monotonically frequency profile in time (linear, first order), starting at about 100Hz until 1,000 – 2,000Hz. As mentioned, this feature has been identified as the “g-mode” of the PNS, but it is not clear that this feature contains only information about the g-mode. The difficulty is that, without a multimodal analysis, this HFF cannot be unequivocally associated with the g mode because it could include both f and g modes [7], or even multiple g-modes [5]. Then, adopting the same convention as that adopted in [8], here we refer to this feature as the High Frequency Feature, HFF, hereinafter.

Previous studies have focused on characterizing the HFF. In Lin et al. [9], a chi-squared optimization was applied in order to find the (first-order) slope and the initial frequency of the HFF. This analysis was performed with O3 LIGO (L1, H1), Virgo (V1) data and TF pixels of 3D CCSN waveforms detected by the Coherent WaveBurst (cWB) pipeline. In Bruel et al. [10], a polynomial fit was applied to estimate the HFF and, subsequently, to infer the evolution of the combination between the mass and the radius of the PNS. This study drew on CCSN waveforms embedded in Gaussian colored noise. More recently, in Casallas-Lagos et al. [8], an optimized regression deep neural network (fully connected) is applied to estimate the (first-order) slope of the HFF. They used O3 LIGO data and TF pixels of phenomenological and general relativistic CCSN GW signals detected by cWB.

Focusing on understanding the occurrence of the HFF rather than inferring parameters to model it by a specific function, in this work we present a new methodology to classify TF image samples (Morlet wavelet scalograms) containing the HFF, depending on the (first-order) HFF slope. In particular, we applied a multi-class classification with three target labels for three consecutive, mutually exclusive intervals in which the HFF slope can be located. Moreover, to reach highly accurate rates and to favor the reproducibility of our results, we draw on one of the state-of-the-art and open-source architectures in computer vision, namely Residual Neural Networks, in particular, ResNet50 [11].

As characterizing the HFF is an inverse problem, the very first step is to address the detectability of the HFF. This is because the recovery of HFF from noisy interferometric data is not guaranteed beforehand in all situations. Once a suitable conversion from strain time series is chosen, the visibility of

the HFF in the TF representation can vary greatly. This variation depends not only on the nature of (and the distance from) the emitting CCSN but also on the noise realization and the properties of the reconstruction algorithms themselves. Moreover, in the context of our supervised machine learning algorithm, if the visibility of the HFF is decreased in a group of samples, the detectability can also decrease and, subsequently, statistically affect the predictions for the whole dataset. From an instrumental point of view, and by applying our multi-class classification strategy, we aim to understand how the previously mentioned factors influence the recognition of the HFF in the CCSN GW signals.

For this work, we consider, as datasets, only TF samples with noise plus GW signals, with the HFF being present. Besides, we used two types of waveforms. To optimize, train and test our ResNet50 algorithm, we first draw on samples of phenomenological waveforms [12] injected into real noise data from L1, H1, and V1 obtained from O3b run, which is freely available on the Gravitational Wave Open Science Center (gwosc.org). These waveforms are generated by a stochastic toy model that, in the TF representation, mimics the HFF. Then, applying our optimized ResNet50 model, we performed a final test on a different dataset formed by multidimensional general relativistic CCSN waveforms injected into real noise data from the L1, H1, and V1 from the O3b run. This last analysis is crucial because general relativistic signals, obtained from numerical relativity simulations, are the closest to what we expect in future possible detections of real CCSN GW signals. Besides, to explore the ability and limits of the predictive model, we apply this test at three galactic distances: 1, 5, and 10Kpc.

Now, considering the astronomical context in which our work is presented, we stress that the problem of how to tag the input samples following an astrophysically informed approach is a more complicated task. Elucidating the specific physical mechanisms of the PNS by which the HFF slope univocally takes a value (or a range of values) is still an on-going research program [13]. This problem is beyond the scope of our study. However, motivated by descriptive clarity, based on what we know from current CCSNe numerical simulations, and aiming to make strong conclusions about the detectability of the HFF using a ResNet50 classification, we defined the target labels in function of the HFF slope, as follows: Class 1 (Steep), Class 2 (Moderate), and Class 3 (Low). In subsection 2.3 we detail the specific HFF slope ranges.

This choice is general enough to go beyond the classic binary classification, which, at this point, could be not very interesting, but also economical

enough to not needlessly increase the labels given the current state-of-the-art physical studies about the HFF. Anyway, as the theoretical understanding of this feature increases, the astrophysical importance of this classification is that, as a proof of principle, it allows us to evaluate our ability to discriminate between CCSN parameter configurations (expressed in HFF slope ranges) that are potentially discoverable through future LIGO and Virgo observations. Moreover, given that we still do not have theoretical certainty about the continuity and/or discontinuity of the HFF slope values, using a classification is the most natural option. If future research, for instance, were to reveal prohibited values (or ranges of values) for the HFF slope, this would not violate any methodological assumption of our classification strategy.

All computer implementations of this work were made by using open-source software: Python v3.9.7 (run locally), Python v3.10.12 (run on Google Colaboratory), TensorFlow v2.15.0, Keras v2.15.0, scikit-learn v1.2.2, SciKeras v0.12.0, Pillow v9.4.0, and PyCBC v2.3.0, among others. Following an open knowledge research philosophy, we make the deep learning code freely available in the public GitHub repository **resnet50-sngw-hff**, in addition to **datagen-sngw-phen** and **datagen-sngw-genrel** containing the dataset generators with phenomenological and general relativistic waveforms.

The paper is organized as follows. Section 2 introduces the problem statement and our methodology, namely: description of real interferometric noise segments and waveforms to be used in the analyzes (both phenomenological and general relativistic waveforms), injection procedure, data conditioning, dataset generation, and the ResNet50 architecture. Later, Section 3 presents our results, separating them into those we obtained working with phenomenological waveforms (Subsection 3.1) and those we obtained by considering general relativistic waveforms (subsection 3.2). In the first subsection of the results, we include specific details about the optimization of ResNet50 through a **GridSearchCV** procedure and subsequent training and testing using the dataset of TF image samples containing interferometric noise plus phenomenological waveforms. Next, in the second subsection of the results, we present the predictions of classifying TF image samples containing interferometric noise plus general relativistic CCSN waveforms by applying our optimized ResNet50 model. In addition, we present a detailed interpretation of the predictions based on the statistical information coming from the injected signal populations. Finally, Section 4 is for conclusions.

2. Methodology

2.1. Problem statement

In this work, the general goal is to classify samples of interferometric data containing the HFF, which entails that we dispense with the task of GW searching and/or trigger generation. As a starting point, we have a raw strain time series described by the expression:

$$s_{raw}(t) = [s(t_0), s(t_1), \dots, s(t_{N_{slice}-1})]^T . \quad (1)$$

Eq. 1 describes a single-interferometer response signal that contains non-Gaussian, non-stationary noise and a certain number of CCSN GW signals added to that noise. Then, the problem is to extract window samples around these signals to classify each of them as belonging to class 1, 2, or 3, depending on the HFF slope of the embedded signal. For this classification, we apply an optimized ResNet50 algorithm.

To address the above problem, we have two high-level stages with their own sub-methodologies. Firstly, the dataset generation, which involves the injection procedure in single-interferometer noise data (independent of other detectors), data conditioning, and the construction of our TF image datasets. And secondly, the classification, which involves the application of the ResNet50 algorithm: optimization, training, and testing with the TF image datasets, and the subsequent evaluation and interpretation of the predictions.

2.2. Noise segments

We consider data segments of real noise from LIGO and Virgo detectors both for training and testing the ResNet50 algorithm. Their time duration and sampling frequency are $t_{N_{slice}} = 4,096$ s and $f_s = 4,096$ Hz, respectively. Then, in consistency with Eq. 1, we describe each data segment as a column vector of $N_{slice} = t_{slice}f_s$ elements.

To explore the sensitivity of a detector, we computed the Amplitude Spectral Density (ASD) of their entire output data segment. We implemented the standard Welch method [14], applying Hanning-windowed segments of 4s with overlapping of 2s along the frequency domain from 0Hz to 2048Hz, with frequency bins of 0.25Hz. ASD plots, in the frequency region from $f = 9.5$ Hz to 1100Hz, are shown in Fig. 1, considering three noise segments: two of the LIGO detectors and one of the Virgo detector. We can refer to this ASD estimate as global because we are considering the whole interferometric data

segment of 4.096s. However, we can also perform a local ASD estimate by considering a window of a few seconds (or milliseconds) around an embedded (injected) GW signal, which is useful for computing the signal-to-noise ratio (SNR) of that signal. The second case will be detailed later.

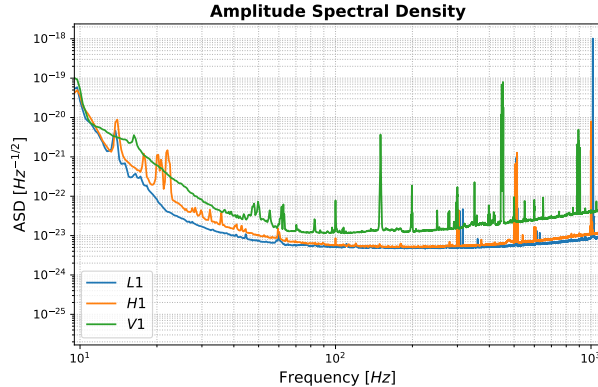


Figure 1: Amplitude Spectral Density (ASD) computed from H1, L1, and V1 noise data. For these estimates, we consider raw strain data segments of $t_{slice} = 4,096$ s, starting at GPS time 1257050112, and sampled at $f_s = 4,096$ Hz.

To generate a sufficient number of window samples as described in sections 2.5 and 2.7, we drew on two noise data segments of time length $t_{slice} = 4,096$ s from the O3b run, with initial GPS times 1256783872 and 1257050112 per each detector.

2.3. Phenomenological waveforms

Taking the approach first proposed in [12] and that we later implemented in [15], we draw on phenomenological parametrized CCSN waveforms for training, validating, and testing the ResNet50 algorithm. These waveforms come from a simplified non-physical model that mimics one of the features that is common to all CCSN simulations, namely the HFF. In the time-frequency representation (for instance, spectrograms or scalograms), the HFF usually appears as an increasing arch.

Phenomenological waveforms can be generated with the equation for the damped harmonic oscillator with random forcing, expressed as follows [12]:

$$\frac{\partial^2 h}{\partial t^2} + \frac{\omega(t)}{Q} \frac{\partial h}{\partial t} + \omega(t)^2 h = a(t), \quad (2)$$

where h is the mimicked strain, $\omega(t)$ the excited eigenmode (angular frequency) of the PNS, Q a constant quality factor, and $a(t)$ a random acceleration. The frequency $f(t) = \frac{\omega(t)}{2\pi}$ is modeled as a 2nd order polynomial:

$$\begin{aligned} f(t) &= f_0 + f_1(t - t_{ini}) + f_2(t - t_{ini})^2, \\ t &\in [t_{ini}, t_{end}] . \end{aligned} \quad (3)$$

where t denotes the time, and t_{ini} and t_{end} the initial and end times of the signal, respectively. Given the external force (particularly $a(t) = a_n\delta(t - t_n)$ with $n = 1, 2, \dots, f_{driver}(t_{end} - t_{ini})$ and a_n randomly distributed on $[t_{ini}, t_{end}]$ and $[0, a_{max}]$, respectively), and rewriting Eq. 3 with $f_1 = f_{1s} = f(t = 1s)$, and $t_2 = \text{argmax}[f(t)]$ ($t_2 > t_{end}$), this system can be numerically solved once we choose initial values for the 7 free parameters: t_{ini} , t_{end} , f_0 , f_{1s} , t_2 , Q , and f_{driver} .

To categorize the waveforms, we defined three classes, depending on the numerical range in which the slope of the HFF for each waveform belongs to:

- **Class 1:** $1,620 \leq \text{HFF slope} < 4,990$ (Steep)
- **Class 2:** $1,450 \leq \text{HFF slope} < 1,620$ (Moderate)
- **Class 3:** $950 \leq \text{HFF slope} < 1,450$ (Low)

This categorization will also be applied to the general relativistic waveforms detailed in section 2.4.

Fig. 2 shows three samples of phenomenological waveforms, one of each class, plotted as strain time series with their respective time-frequency Morlet wavelet scalograms (in section 2.7 we briefly describe how these scalograms are generated). Notice from the strain time series that the duration of waveforms varies, which is expected because of the random force component of the model. Moreover, from the scalograms we observe how the HFF slope is clearly different among the three waveform samples.

For the analysis, we draw on 600 phenomenological waveforms, 200 per class, which will be randomly injected into the noise segments. Section 2.5 describes the procedure to perform these injections.

2.4. General relativistic waveforms

In this work, we considered three CCSN waveforms that are openly distributed. These waveforms have HFF slopes that belong to the classes defined in Eq. 2.3 (one waveform per class), in addition to other features such

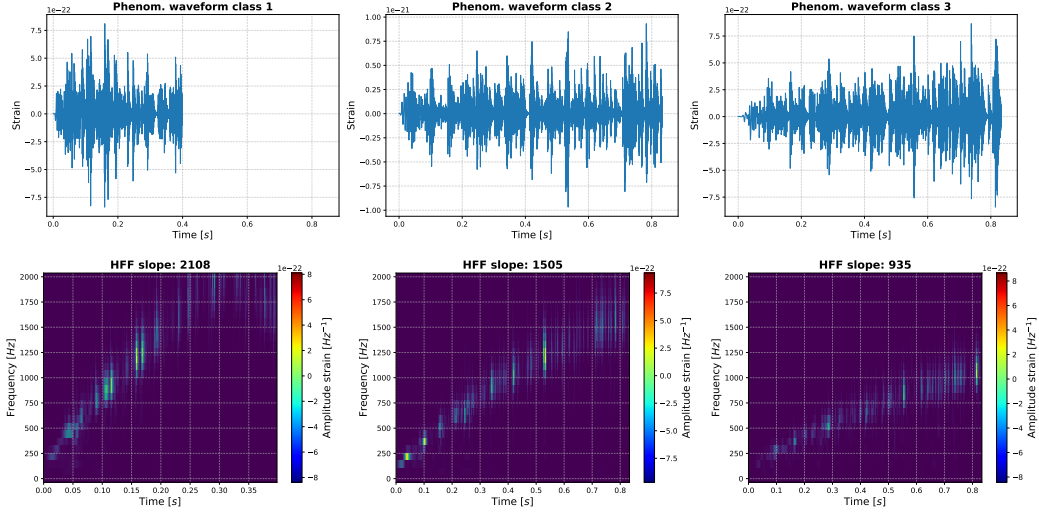


Figure 2: Three phenomenological waveforms in the time domain (upper panel) and their Morlet wavelet scalograms (bottom panel). Depending on their HFF slope, these waveforms belong to classes 1, 2, and 3. For the HFF slope 2108, $f_0 = 126.63\text{Hz}$ and $f_1 = 3416.08\text{Hz}$; for slope 1505, $f_0 = 108.14\text{Hz}$ and $f_1 = 1774.62\text{Hz}$; and for slope 935, $f_0 = 105.28\text{Hz}$ and $f_1 = 1148.24\text{Hz}$.

as the standing accretion shock instability, usually referred to as SASI, and the prompt-convection feature.

- Andresen et al. 2019 3D, *m15nr h+* [16]. Model of a $15M_\odot$ non-rotating progenitor constrained by a Lattimer and Swesty equation of state (EoS) with nuclear compressibility $K = 220\text{MeV}$ (LS220). Strong SASI activity dominated by the spiral mode, prompt convection, and the HFF are produced.
- Morozova et al. 2018 2D, *M13_SFHo h+* [7]. Model of a $13M_\odot$ non-rotating progenitor constrained by the Steiner (SFHo) EoS. Weak SASI activity, prompt-convection, and the HFF are produced.
- Cerdá-Durán et al. 2013 2D, *fiducial* [17]. Model of a $35M_\odot$ rapidly rotating progenitor, constrained by the LS220 EoS. Weak SASI activity, prompt-convection, and the HFF are produced.

Fig. 3 shows the three general relativistic waveforms used in this work, both in the time domain (strain) and in the time-frequency domain (Morlet wavelet scalograms). As shown in the bottom panel, SASI activity appears in the region below the early times of the HFF, and the prompt-convection feature approximately appears during the first 0.1 seconds after the bounce.

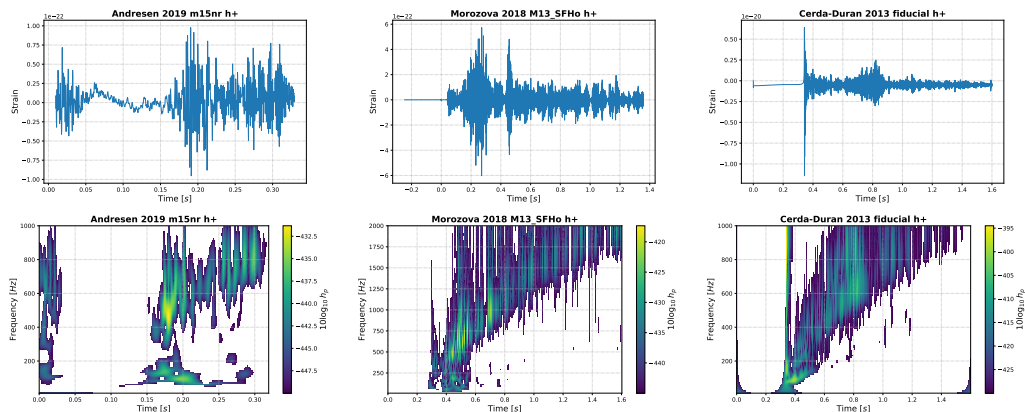


Figure 3: General relativistic CCSN waveforms simulations used in this work, both in the time domain (upper panel) and their Morlet wavelet scalogram representation (bottom panel). These plots describe the waveforms solely, i.e., without noise. Andresen et al. waveform comes from a 3D CCSN simulation, and Morozova et al. and Cerdá-Durán et al. waveforms come from 2D CCSN simulations. To see the features more clearly, the power amplitude is shown using a logarithmic scale.

A necessary procedure was needed to estimate the HFF slope of each waveform. To accomplish this estimation while minimizing ambiguity, we proceeded to isolate the contribution of the HFF as follows: after converting strain series to TF scalograms, we represent these scalograms as pixel scatter plots. Then, the wavelet removal is performed using a three-step methodology. Firstly, we compute a wavelet threshold defined as the arithmetic mean of all wavelets in the scatter plot, and we remove the pixels with intensity lower than that mean. Secondly, we remove the pixels from the initial time to 0.1s for the Andresen and Morozova waveforms and to 0.4s for Cerdá-Durán waveform; these are the regions where the prompt-convection feature appears. Finally, we remove pixels located at frequencies less than 250Hz, which is the region where SASI appears.

CCSN waveform	HFF slope [Hz/s]	HFF intercept [Hz]	R^2	Class
Andresen 2019 <i>m15nr h+</i>	2601.99	36.4985	0.78906	1
Morozova 2018 <i>M13_SFHo h+</i>	1451.37	-58.9381	0.93960	2
Cerdá-Durán 2013 <i>fiducial h+</i>	956.261	-112.200	0.77444	3

Table 1: HFF slope estimates for the three general relativistic CCSN waveforms used in this work. These results were computed in the absence of noise after removing the contributions of wavelet features other than the HFF.

After removal of the above wavelets, we estimate the slope of the HFF. For this, we apply a linear regression, considering the most energetic pixels each time. The results for the HFF slope estimation, for the three CCSN GW signals, are detailed in Fig. 4 and Table 1.

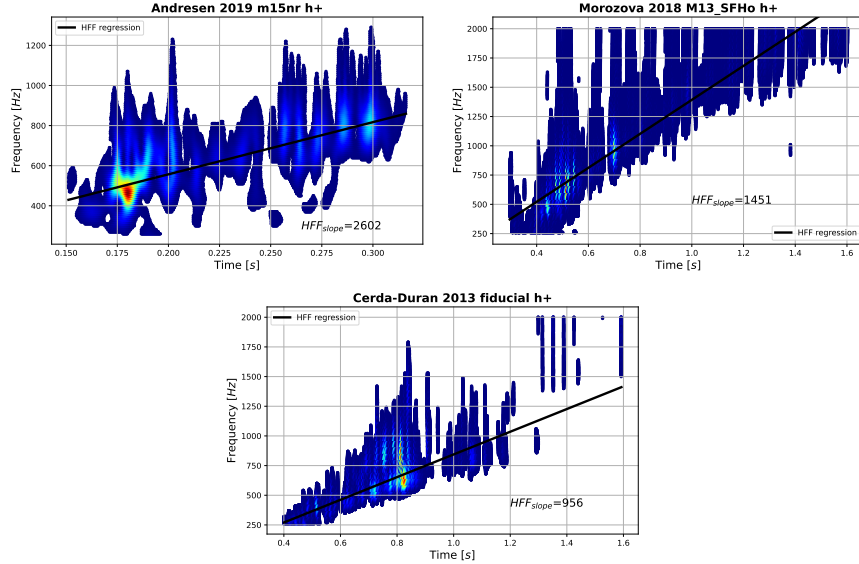


Figure 4: HFF slope estimation for CCSNe numerical waveforms, using linear regression. Before this fit, wavelet contribution of the background (arithmetic mean of all pixels), and wavelet contributions from features other than the HFF, were removed.

As shown in Fig. 2, the morphology of phenomenological waveforms in the TF scalograms is such that their only feature is the (mimicked) HFF. For

all phenomenological waveforms that we used, the HFF begins at the left-bottom corner of the scalogram, i.e., at the very beginning of the waveform. However, this is not the case for general relativistic waveforms, as can be noticed in Fig. 3, in which the initial time of the HFF is not the same, and there are other features that can be observed in the TF scalograms. This discrepancy poses two aspects that we decided to address before injecting general relativistic waveforms into noise data to be consistent between training and test datasets.

Firstly, we set the initial time of the general relativistic waveforms such that the HFF begins approximately at the beginning of the waveform. Until now, there is not an established methodology to estimate the initial time of the HFF. Then, simply by visual exploration, we selected a left region of the waveform (in the time domain) to remove until the HFF, approximately, appeared. For Andresen 2019 *m15nrh+*, we remove the first 0.16s; for Morozova 2018 *M13.SFHo h+*, the first 0.30s; and for Cerdá-Durán 2013 *fiducial*, the first 0.38s.

The next procedure is to remove the contribution of features other than HFF from the cropped waveform. The prompt-convection feature was already removed with the early times cropping previously applied. To remove the SASI feature, on the other hand, we applied a Butterworth high-pass filter with a critical frequency of 250Hz. Bear in mind that this feature removal is different from that we performed for the HFF slope estimation; here, we apply editions in the time domain, and we do not isolate the HFF.

2.5. Injection procedure

We consider a single-interferometer noise segment that can be described by the time series:

$$n(t) = [n(t_0), n(t_1), \dots, n(t_{N_{slice}-1})]^T, \quad (4)$$

which, as mentioned in section 2.2, has a sampling frequency $f_s = 4,096\text{Hz}$ and time duration $N_{slice}/f_s = 4,096\text{s}$.

Next, we define a non-uniform time sequence to localize injections along the described single-interferometer noise segment. In particular, we consider a time sequence with a fixed difference $\Delta t_{inj} = 8\text{s}$ randomly modified such that each i -th injection ($i \neq 0$) is located at the time:

$$t_{inj_i} = t_{inj_0} + i\Delta t_{inj} + jitter_i, \quad (5)$$

where $jitter_i = random_i([-0.1, +0.1])$ and t_{inj_0} is the time location of the first injection.

As we will extract time windows of the same length (see section 2.7), term $jitter_i$ is included in Eq. 5 to avoid the ResNet50 algorithm mislearns the HFF characterization based on a fixed location of the GW signals in the windows.

Whether we are working with phenomenological or modified general relativistic CCSN waveforms, the injection procedure is applied such that we inject waveforms of only one class in each single-interferometer data noise segment of 4,096s (either from LIGO or Virgo).

Setting the input parameters as mentioned earlier ($\Delta t_{inj} = 8\text{s}$ and $jitter_{lim} = 0.01\text{s}$), we perform 511 injections of phenomenological waveforms in a noise segment of 4,096s. As previously mentioned in section 2.2, we draw on two noise segments of 4,096s, which entails $511 \times 2 = 1,022$ injections per class. Because of the three classes, we work with a total of $1,022 \times 3 = 3,066$ injections per detector per class, resulting in a total of $3,066 \times 3 = 9,198$ injections considering all three detectors (L1, H1, and V1).

It is important to highlight that, once the time window samples were generated (as detailed in Section 2.7), they were slightly less than the aforementioned number of injections. This is because we removed some window samples that depended on specific conditions for the SNR values.

In the case of general relativistic waveforms, we set the same input parameters and obtained the same number of injections as in the case of phenomenological waveforms. However, we considered only 100 window samples per class per noise segment, which is enough for testing purposes. Bear in mind that we want to train the ResNet50 algorithm solely with phenomenological waveforms (as detailed in Section 3.1), which are much simpler in terms of information content and generation.

2.6. Data conditioning

After injecting the waveforms, we generate raw strain data segments $s_{raw}(t)$, which are described in Eq. 1. Then, to perform data conditioning, we followed a two-step standard methodology in LIGO-Virgo pipelines, namely: i) whitening and ii) band-pass filtering. To implement this methodology, we applied some functions contained in the PyCBC library [18].

Whitening allows us to approximate detector noise to a Gaussian stochastic process. For this, we attenuated the Fast Fourier Transform of $s_{raw}(t)$ by its ASD in the frequency domain, using the same configuration as in the noise

exploration detailed in section 2.2: 4s segments windowed with the Hanning function, overlapping by 2s, in a frequency domain from 0Hz to 2048Hz, with 0.25Hz of resolution. As whitening generates spurious frequencies on the edges of the data segment due to spectral leakage, we removed 5s of the data at each edge.

After whitening, we applied a high-pass and a low-pass Butterworth filter, both of 8th order, to remove frequency components lower than 100Hz and higher than 1800Hz, respectively.

2.7. Dataset generation

2.7.1. Strain window samples

After conditioning, we have data segments $s_c(t)$ that can be described by:

$$s_c(t) = [s_c(t_0), s_c(t_1), \dots, s_c(t_{N_c-1})]^T, \quad (6)$$

where $N_c < N_{slice}$ because edge data removal after whitening. Then, we have that the number of injections in the segment $s_c(t)$ is $N_{inj}^c \leq N_{inj}$, depending on the durations of GW signals and the chosen time distance between each injection. Then, for the strain dataset generation, we extracted windows samples of time duration, $T_{win} < N_c/f_s$, from the data segment described in Eq. 6. For simplicity, we required that each window sample has only a whole injected phenomenological GW signal (independent of $jitter_{lim}$, Δt_{inj} , and Δh_j); hence, we impose two constraints detailed below.

Firstly, we impose that:

$$T_{win} = \Delta h^{max} + \alpha, \quad (7)$$

where Δh^{max} is the duration of the longest injected phenomenological waveform, and α is an input parameter greater than $2jitter_{lim}$ which we set as $\alpha = 0.02001$.

The second constraint had to do with the initial time of window samples, and this is:

$$T_{win_j}^{start} = t_{inj_j} + \frac{1}{2}(\Delta h_j - T_{win}) - jitter_i, \quad (8)$$

where it can be seen that if $jitter_{lim} = 0$, then $jitter_i = 0 \forall i$, and consequently, all injections are centered in their respective window samples. But, as mentioned earlier, if we want to work with $jitter_{lim} \neq 0$, then Eqs. 7 and 8 are well general enough.

Given that Δh^{max} is computed only with phenomenological waveforms varying from 0.3s to just under 1.0s (see center panel of Fig. 5), the condition of having a whole injection in each window may be violated when working with general relativistic waveforms. In particular, we observed this violation with Morozova *M13_SFHo h+* and Cerdá-Durán *fiducial* waveforms, which have durations longer than 1s before pre-injection modification. In such cases, the portion of the waveform that is outside is very small; therefore, this violation was not a problem for our analysis.

2.7.2. Wavelet Transform

The next step is to convert each p -th strain window sample, say s_{win}^p , to a TF scalogram using the Morlet Wavelet Transform (WT). Then, now is the moment to briefly explain how we computed these scalograms.

In general, a WT requires a kernel (i.e., a localized “mother wavelet”), which, varying its location and scale, is convolved with the window samples to scan frequency changes in the signal. For our study, we drew on a Morlet wavelet [19] as the kernel, which we also used in a previous study [20]. This is defined as follows:

$$\psi(t_j, f_k) = \frac{1}{\sqrt{\sigma_j^t} \sqrt{\pi}} \exp \left[\frac{-t_j^2}{2(\sigma_j^t)^2} \right] \exp(2i\pi f_k t_j) , \quad (9)$$

which has a 2D Gaussian form, with standard deviations σ^t and σ^f , related by $\sigma_j^t = 1/(2\pi\sigma_j^f)$ and $\sigma_j^f = f_l/\delta w$, where δw is the wavelet’s width (that we set beforehand in 7Hz) and f_k its center in the frequency domain. Subsequently, to generate the TF scalogram of a s_{win}^p window sample, we compute:

$$W_{s_{win}^p} [t_n, f_j] = \sum_{m=0}^{N_{win}-1} s_{win}^p(t_m) \psi^*(t_{m-n}, f_j) , \quad (10)$$

where $s_{win}^p(t_m)$ is the element m of the column vector s_{win}^p . Besides, we have that $n = 0, 1, \dots, N_{time}$ and $j = 0, 1, \dots, N_{freq}$, where N_{time} and N_{freq} define the size of each 2D matrix generated by the WT, being $W_{s_{win}^p} [t_n, f_j]$ the (n, j) element or of it.

Notice from Eqs. 9 and 10 that ψ and $W_{s_{win}^p}$ need to be defined over a finite grid containing discrete values of time and frequency. For our implementation, we define a time vector taking values from $t_0 = 0$ to $t_{N_{time}} = T_{win}$

with $\delta t = 1/f_s$. Besides, we set $f_{ini} = 10\text{Hz}$, $f_{end} = 2000\text{Hz}$, and $\delta f = 10\text{Hz}$ for the initial frequency, the final frequency, and the frequency resolution, respectively. Finally, the WT transform is such that its matrix has dimensions $N_{time} = T_{win}/\delta t = 3971$ and $N_{freq} = (f_{end} - f_{ini})/\delta f + 1 = 200$.

2.7.3. Sample images datasets

The methodology continues by converting the window strain samples to RGB sample images. A direct conversion from the actual WT numerical matrix to pixelized images would entail images of dimensions of 3971×200 pixels. Working with such images would take a lot of resources, storage, and memory. Then, to minimize resources, we draw on the Pillow (PIL Fork) image module [21], and apply a resizing to output pixelized images of dimensions $N_{time} = 64$ and $N_{freq} = 64$. Now, the ResNet50 architecture is designed to input RGB colorized images by default (in three channels), and we decided to maintain this for practical purposes. Then, we also apply Pillow to set the final dimensions of each TF sample image as $64 \times 64 \times 3$ by copying the pixel value of a grayscale image into their respective pixels in red (R), green (G), and blue (B) channels. This implementation is general enough to be potentially included in a broader pipeline that, in a first stage of GW detection (in which it would be desirable to include consistency of a signal between the detectors of the network), the RGB input can easily be adapted to include simultaneous samples of H1, L1, and V1 detectors (for instance, as proposed in [12]), without modifying our current ResNet50 architecture.

Finally, after all previous procedures, our final datasets can be written as:

$$D = \{ \mathbf{X}^{64 \times 64 \times 3}, \mathbf{y}_c \}^{N_s}, \quad (11)$$

where N_s denotes the number of image samples for the class y_c .

Working with phenomenological waveforms, the dataset is formed as follows. With L1 data, we have $N_s = 1,020$ for $y_c = 1$, $N_s = 1,017$ for $y_c = 2$, and $N_s = 1,013$ for $y_c = 3$. With H1 data, $N_s = 1,013$ for $y_c = 1$, $N_s = 1,012$ for $y_c = 2$, and $N_s = 1,011$ for $y_c = 3$. And finally, with the V1 data, we have $N_s = 1,021$ for $y_c = 1, 2, 3$. As it is described in section 2.7.4, we used data from all interferometers, all together, to optimize the ResNet50 architecture.

On the other hand, with general relativistic CCSN waveforms, the datasets are smaller: $N_s = 100$ for $y_c = 1, 2, 3$ at one distance. Then, for the three chosen distances (1Kpc, 5Kpc, and 10Kpc), we have a total of $100 \times 3 \times 3 = 900$ image samples.

We finally mentioned that, before being inputted into the ResNet50 algorithm, we had to apply a last preparation to our dataset to facilitate processing and learning. Firstly, we normalize all our image samples such that each pixel has a value between 0 and 1; this is achieved by simply dividing each original pixel value by 255. Next, we convert all target labels from categorical values to $1D$ vectors according to one-hot encoding.

2.7.4. Injected phenomenological signals populations

Now we present an exploration of the dataset for the optimization of the ResNet50 algorithm. This dataset consists of samples containing noise plus phenomenological waveforms, with noise data from the L1, H1, and V1 detectors, all together.

The upper left and upper right panels of Fig. 5 show the distribution of their HFF slopes and time durations in the absence of noise, respectively. These are actual values before being injected into the noise. Notice that the HFF slopes (and therefore the class of GW signal samples) are distinguishable, with reduced populations of slopes around the critical values between classes. Moreover, we can also see that a distribution of waveform durations for one class overlaps with at least one other distribution.

With regards to waveform durations, we can also observe that variation of the duration is expected because of the stochasticity of our generating toy model. We can also observe that class 1 waveforms tend to have shorter durations in comparison to class 2 and class 3 waveforms. To some extent, this difference is because class 1 waveforms have greater slope values, which implies that the HFF reaches the frequency limit more rapidly in comparison to class 2 and class 3 waveforms.

Finally, bottom panel of Fig. 5, on the other hand, shows the distribution of SNR values of phenomenological waveforms after being injected into L1, H1, and V1 noise data segments. Here, it should be mentioned that, once the time window samples with injections were generated, we imposed the constraint that SNR do not exceed the value of 100; i.e., if this happened for a specific window sample, we simply removed it from our dataset.

We emphasize that working in the high SNR regime, with phenomenological waveforms, is for the sole purpose of facilitating the HFF learning process. However, once the algorithm is optimized, we need to test it in a more realistic situation to reach solid conclusions. This will be shown later.

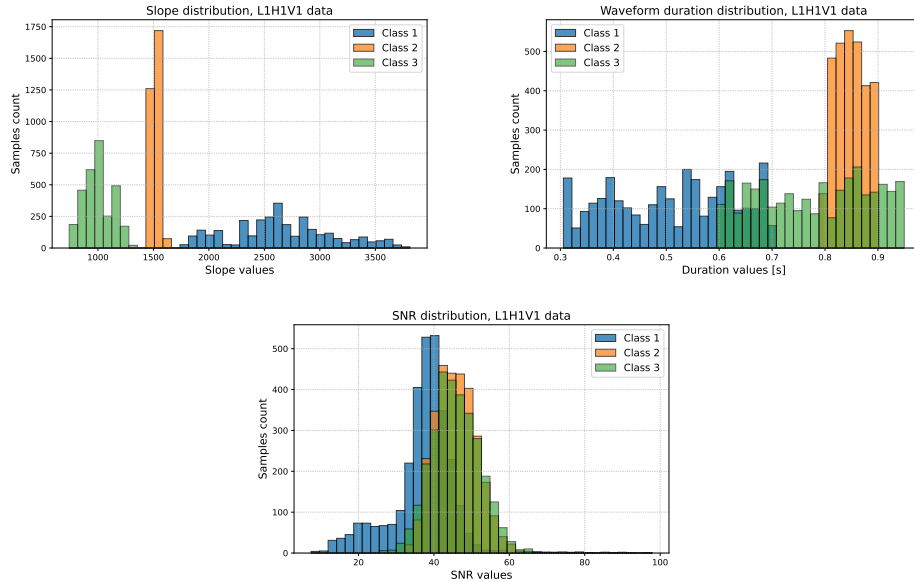


Figure 5: Distribution of the HFF slope (upper left panel) and duration (upper right panel) of the phenomenological waveforms before being injected in (and recovered from) all noise data segments. These waveforms were generated by a stochastic model and their duration varies from 0.3s to just under 1.0s. In addition, SNR values distribution of time window samples used for training and testing the ResNet50 are shown (bottom panel). SNR distribution for class 1 samples is shifted to lower SNR values in comparison to SNR distributions for class 2 and 3 samples. SNR values greater than 100 were excluded.

2.8. ResNet50 architecture

As it were first introduced and shown by He et al [11], residual deep networks reach greater performance results than those reached by shallower standard CNN architectures such as LeNet, AlexNet, and VGG. Before residual networks were invented, CNN architectures exposed a problem of degradation in train and test accuracy as more and more layers were added (namely, surpassing a few tens of layers), even if these layers gave an identity mapping to reproduce a deep solution by construction. The proposed residual framework finally solved this problem, allowing us to implement CNN architectures with a very large number of hidden layers (tens, hundreds, or even thousands of layers), and its core idea is as simple as ingenious, as we briefly describe below.

Let be stacked nonlinear layers that input data \mathbf{x}_{in} . In this scenario, what

traditionally would learn about the layers is the original mapping $\mathcal{M}(\mathbf{x}_{in})$. However, under this new benchmark, the layers learn instead the residual mapping \mathcal{R} , being related to the original mapping by:

$$\mathcal{M}(\mathbf{x}_{in}) = p(\mathbf{x}_{in}) + \mathcal{R}(\mathbf{x}_{in}, \mathbf{W}) , \quad (12)$$

where \mathbf{W} is the matrix codifying the weights and biases present in the layers, and p is a function of input data operating parallel to the main pathway, as it is shown in the two situations depicted in Fig. 6. Consequently, the output of the stacked layers along the main path is as follows:

$$\mathbf{x}_{out} = f_{out}(\mathcal{M}(\mathbf{x}_{in})) , \quad (13)$$

where f is the last activation function, which we choose beforehand as the Rectified Linear Unit (ReLU).

Eq. 12 is called the “skip connection”, explicitly involving the term $p(\mathbf{x}_{in})$ which codifies the structure of the connection. More generally, Eqs. 12 and 13 together are called “Residual block” or “Residual unit”. To ensure that operations in these equations for a residual block are correctly defined, we need to satisfy a crucial condition, namely that the dimension of activation f_{in} (where data \mathbf{x}_{in} come from before inputted into the residual block) and f_{out} must be the same. Let us call this the “in-out dimensional” condition.

Fig. 6 shows two basic residual blocks, which are both formed by two paths. A main path is common to both blocks, which have three 2D Convolutional layers, including Batch Normalization (BN) and a ReLU layer. In addition, there is a secondary path describing the skip connection itself, which needs to fulfill the in-out dimensional condition. On the left panel, we have an identity skip connection, which is applied when \mathbf{x}_{in} data inputted by the first Convolutional layer in the main path have the same dimension as the data inputted to the third activation layer. We call this block “Identity Block” (Id Block). On the other hand, the right panel shows a 2D Convolutional skip connection, which is applied when the dimensions of the mentioned data are not the same. We call this block “Convolutional Block” (Conv Block).

Now that we have already explained the structure of the basic building blocks, Id Block and Conv Block, we present in Fig. 7 the general architecture used in this work, namely ResNet50. The number 50 in his name is because this deep network has 50 parameter layers in the main path, and these layers are distributed in 5 stages in addition to the classification. Take in mind that

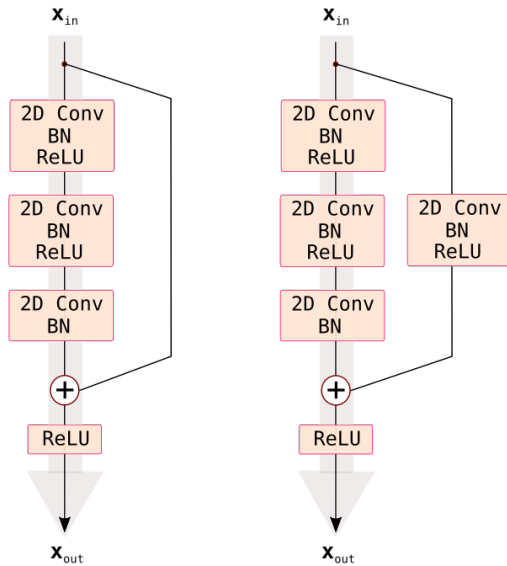


Figure 6: Basic residual blocks. Left panel: Identity Residual Block, in which its input data is directly added to the output of the third convolutional stack in the main path. Right panel: 2D Convolutional Residual Block, in which its input data passes through a Convolutional layer in the secondary path such that the dimensions before and after the first and third Convolutional layers of the main path, respectively, are the same.

Id Block and Conv Block, as shown in Fig. 6, have three parameter layers; therefore, we have 48 main parameter layers from stage 2 to stage 5, which are added to one layer in stage 1 and another layer in the classification.

ResNet is a well-known (and well-tested) architecture in the Machine Learning community [22], and the ResNet50 benchmark has a predefined configuration of hyperparameters. For this study, we considered that predefined configuration, which is shown in Table 2. In addition to those settings, we consider a zero padding of dimension 3×3 after inputting data, a max pooling of 3×3 with stride 2 after stage 1, and an averaging pooling of 2×2 after stage 5 of the ResNet50 model.

Our ResNet50 implementation was made by using the TensorFlow software library [23] and Keras interface[24]. In the section 3 we will give details about the optimization, training, and testing of the ResNet50.

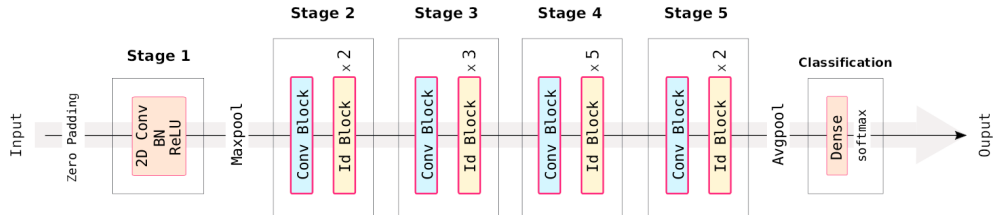


Figure 7: ResNet50 architecture. This is formed by five stages in which identity blocks and/or convolutional blocks are applied, plus a classification stage with a dense (fully connected) layer with a softmax activation giving three probabilistic scores per class. Besides, after stages 1 and 5, a max pooling and an average pooling, respectively, are applied to reduce the system resources. Also notice that at the beginning, a zero padding is applied to the input data.

Information	Stage 1	Stage 2	Stage 3	Stage 4	Stage 5	Classification
Kernels dim; # filters (per block)	$7 \times 7; 64$	$1 \times 1; 64$ $3 \times 3; 64$ $1 \times 1; 256$	$1 \times 1; 128$ $3 \times 3; 128$ $1 \times 1; 512$	$1 \times 1; 256$ $3 \times 3; 256$ $1 \times 1; 1024$	$1 \times 1; 512$ $3 \times 3; 512$ $1 \times 1; 2048$	—
# layers in main path	1	9	12	18	9	1
# layers in skip connections	—	1	1	1	1	—
# parameters	9, 728	220, 032	1, 230, 336	7, 129, 088	14, 998, 528	6, 147

Table 2: Summary of the settings in the ResNet50 architecture that we used in this work. The total number of layers in the main path is 50, and the total number of parameters is 23, 593, 859, occupying 90MB in memory.

3. Results and discussion

3.1. Analyses with phenomenological waveforms

To work with the ResNet50 algorithm, we split the input dataset it into two primary subsets, namely the test set (30%) and the training set (70%).

3.1.1. Sanity Check: Single learning process

As a first experiment, we train the algorithm in a single learning process. For this, we split the training set into two subsets: one for the training itself (90%) and the other for validation (10%) which is a mini-test to monitor the learning in each epoch (one epoch is the time in which the entire training dataset of N_{train} samples passes once through ResNet50). We set an Adaptive Moment Estimation (Adam optimizer) with a learning rate of $\alpha = 0.0005$, batch size of $b_s = 50$, and $n_e = 40$ epochs, obtaining the results shown in Fig. 8 using L1 data (upper panel) and L1, H1, V1 data (bottom panel). These results, which are representative enough of all the cases that we run,

show two important aspects. First, there is no persistent effect of rapid perturbations introduced by batch training, which is good news for stability or our estimates. In addition, we see that good performances are reaching very fast after the 5th – 15th epoch, which is good news for minimizing system resources.

However, we stress that the performance of the ResNet50 does not always improve as we advance in epochs. We can see from Fig. 8 that from the middle to the later epochs the improvement is minimal; even short detrimental effects to the performance can suddenly appear, as can be seen in the case of learning from L1, H1, V1 data. Then, it may happen that once the training is finished, the performance is not the best in comparison to previous epochs. To address this issue (particularly in the final training and test, Section 3.1.3), we will implement a `ModelCheckpoint` callback that, after finishing the training, saves the model of maximum validation accuracy observed along all epochs.

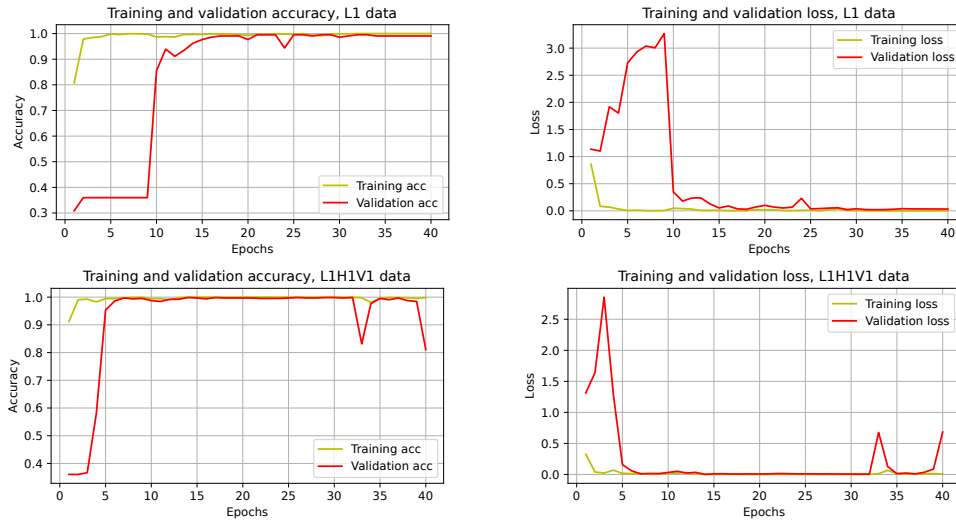


Figure 8: Two representative cases of a single learning process, with image samples of L1 data (upper panel) and combined L1, H1, and V1 data (bottom panel), and injections of phenomenological waveforms. Accuracy (left panel) and categorical cross-entropy, i.e., the loss function (right panel), are shown during the training and validation processes.

3.1.2. *GridSearchCV* tunings

The next step is to apply `GridSearchCV` hyperparameter tuning using the training set. This technique consists of repeatedly applying k-fold cross

validation (CV) to explore the performance of ResNet50 for different combinations of hyperparameters. These combinations are taken from different dictionaries, and once the exploration is finished, we proceed to select the best combination.

Apart from model selection, k-fold CV allows us to address the inherent stochasticity of models by applying resampling and, therefore, to alleviate the artificiality introduced by class-balanced input datasets. K-fold CV, applied to a single model (i.e., a single hyperparameter combination), involves three steps: i) randomly split the training set into k nonverlapping subsets; ii) perform trials in which the i -th subset ($i = 1, 2, \dots, k$) is used for validation and the rest subsets for training; and iii) summarize the performance of the model by computing the average validation loss and average validation accuracy along all trials. It should be mentioned that, unlike a single learning process, in k-fold CV the validation for each fold is applied only once after the training, not for each epoch during the learning.

As shown in Table 2, the ResNet50 has several hyperparameter values that are specific to its architecture by design, i.e., they are predefined: number of layers, kernel dimensions, and number of neurons in specific layers, among others. We decided to maintain these hyperparameters as fixed. However, there are other relevant hyperparameters associated with training that we tuned with `GridSearchCV`, namely: the batch size b_s , the number of training epochs n_e , and its learning rate α and momentum m . Moreover, to take advantage of this tuning procedure, we included another element to tune, which, more than a single hyperparameter, is a process, namely the optimizer. It is a common practice to arbitrarily set the optimizer, but here we want to choose it from a set of different options, motivated by a pure training exploration. (For a recent review of the optimizers chosen for our exploratory set and others, see [25])

With this at hand, we applied three consecutive `GridSearchCV` tunings. In each tuning, we monitor the performance of the ResNet50 by combining some hyperparameter values from one or more dictionaries. By best model, we simply refer to the model in which its accuracy is the greatest in comparison to those of other models, in specific tuning. The hyperparameter dictionaries used in this analysis are the following:

- **Tuning 1**, for optimizer.

$Opt = \text{SGD, RMSprop, Adagrad, Adadelata, Adam, Adamax, Nadam.}$

- **Tuning 2**, for batch size and No. of epochs.

$$b_s = 25, 50, 75, 100.$$

$$n_e = 20, 30, 40.$$

- **Tuning 3**, For learning rate and momentum.

$$\alpha = 0.0005, 0.001, 0.01, 0.1.$$

$$m = 0.0, 0.2, 0.4, 0.6.$$

For each tuning, ResNet50 takes one value from a hyperparameter dictionary; therefore, we have single values in the first tuning and pairs of values in the second and third tunings. As initial hyperparameters, before tuning 1, we set $b_s = 50$, $n_e = 40$, $\alpha = 0.0005$, and $m = 0$. We also chose $k = 5$ for CV, which gives us $n_{fits}^1 = 5 \times 7 = 35$ fits for tuning 1, $n_{fits}^2 = 5 \times 4 \times 3 = 60$ fits for tuning 2, and $n_{fits}^3 = 5 \times 4 \times 4 = 80$ fits for tuning 3. The results are shown in Table 3, in which we can immediately observe that, consecutively, (5-fold CV) mean accuracy increases as we advance to the next tuning. Also note that the mean fit time is relatively similar in tuning 1 and 2, even if tuning 2 is slightly shorter. For these consecutive tunings, we draw on combined data from the three interferometric detectors, L1, H1, and V1.

In terms of computer time and resources, this 3-part tuning was by far the most intensive task that we performed in this study. It was possible using a NVIDIA A100 Tensor Core GPU Architecture, available by upgrading Google Colaboratory, with a 83.5GB system RAM, a 40.0GB GPU RAM, and a disk space of 78.2GB. We can compute the total mean computing time (TMCT) by approximately taking the values in the most-right column of the Table 3 and calculating:

$$\begin{aligned} \text{TMCT} &= \sum_{i=1}^3 n_{fits}^i \times \bar{t}_{fit}^i \\ &= (35 \times 115.1)s + (60 \times 110.8)s + (80 \times 101.5)s \\ &\approx 18796.5s \approx 5.221hr . \end{aligned} \tag{14}$$

In summary, after performing our three GridSearchCV tunings, we find that the best hyperparameter setting to train the ResNet50 is: RMSprop optimizer with learning rate $\alpha = 0.01$ and momentum 0.6, batch size $b_s = 75$, and number of epochs $n_e = 40$.

Tuning	Best hyperparameters	Mean accuracy \pm std	# fits = n_{fits}	Mean fit time = \bar{t}_{fit} (s)
1	RMSprop	0.9943 \pm 0.000884	35	115.1
2	$b_s = 75, n_e = 40$	0.9960 \pm 0.001511	60	110.8
3	$\alpha = 0.01, m = 0.6$	0.9965 \pm 0.001550	80	101.5

Table 3: Results of the `GridSearchCV` tunings applied to the training set, with L1, H1, and V1 data and phenomenological waveforms. As it can be observed, the chosen model, sequentially, is better than the previous. We finally store the set of hyperparameters obtained in tuning 3, to be used in the final training and test in section 3.1.3.

Process	Accuracy	Loss
Train	0.9990	0.002400
Validation	0.9984	0.01700
Test	0.9942	0.03036

Table 4: Metrics obtained after training, validating, and testing the ResNet50 architecture using the best combination of hyperparameters found in `GridSearchCV` tunings. We drew on image samples with noise from detectors L1, H1, and V1 and injected phenomenological CCSN waveforms. We implemented a `ModelCheckpoint` callback to choose the model with maximum validation accuracy across all training epochs.

3.1.3. Training and testing the optimized ResNet50 model

The next analysis is to perform a training and a test using, again, data from the three interferometric detectors all together: L1, H1, and V1. The training set has 70% of the image samples and the test set has 30%. We also maintain the splitting of our training: 90% of the image samples for the training itself and 10% for the validation. Even if we already perform `GridSearchCV`, the validation, in this case, is still useful because, by implementing a `ModelCheckpoint` callback, we will save the model of maximum validation accuracy observed along all epochs once the training is finished. The basic metrics obtained in this final analysis are detailed in Table 4. In addition to that, Fig. 9 shows the confusion matrix for the test analysis, which, as can be observed, the recognition of the three types of samples is excellent.

In terms of computing time and resources, the training was fast and cheap. We used an NVIDIA T4 Tensor Core GPU freely available from Google Colaboratory, with 12.7GB system RAM, 16.00GB GPU RAM, and a disk space of 78.2GB. The total computing time was $344s \approx 5.73min$. Finally, the test was even faster, taking 5s.

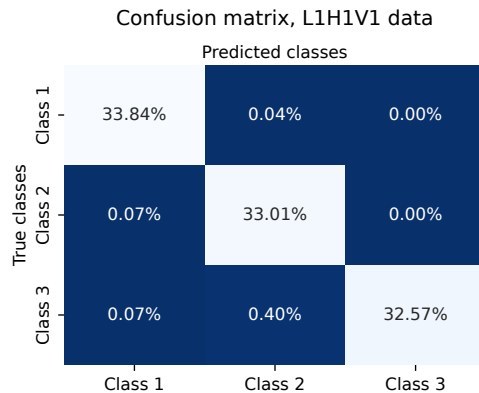


Figure 9: Confusion matrix obtained from testing the best ResNet50 model found with our `GridSearchCV` tunings. Here we drew on image samples containing phenomenological CCSN waveforms injected into noise from detectors L1, H1, and V1.

3.2. Analyses with general relativistic waveforms

3.2.1. Input image samples

Now we present the results of a final test. Here, we applied the optimized ResNet50 model to classify TF image samples with noise plus general relativistic CCSN waveforms. For this task, we considered three different distances from the emitting CCSN: 1Kpc, 5Kpc, and 10Kpc, which are on the order of our galaxy. As previously mentioned, we drew on 100 image samples per class per distance, resulting in a total of $100 \times 3 \times 3 = 900$ TF image samples. Bear in mind that these samples correspond to interferometric noise plus GW signals from one of these three CCSN multidimensional models: Andresen 2019 *m15_{n,r} h+* (3D model, class 1), Morozova 2018 *M13_SFHo h+* (2D model, class 2), and Cerdá-Durán 2013 *fiducial h+* (2D model, class 3).

In Fig. 10 we show representative image samples that were inputted to the trained ResNet50 classifier: one sample per class per distance. Notice that at a fixed distance, the samples have different SNR values and the visibility of the HFF varies. This happens for two physical reasons: the noise realization for each sample is not the same, and GW signals come from different emitting sources, that is, different CCSN numerical relativity models. Now, if we observe samples for a specific model (i.e., a single class), we can observe that as we increase the distance, the HFF feature is less visible. This is expected because, for a given background noise data, the greater the distance from the

emitting source, the smaller the strain magnitude of the signal.

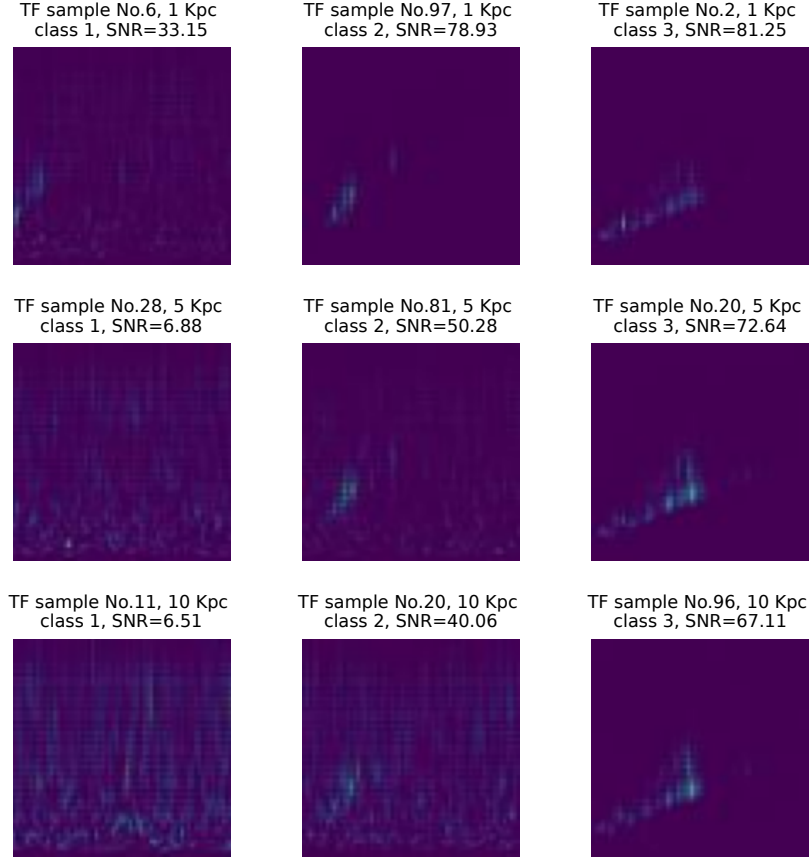


Figure 10: Representative TF scalogram image samples after the RGB pixelization with the PIL Python module. These include L1 interferometric noise plus general relativistic CCSN GW signals injected into interferometric noise from the L1 detector. SNR values and sample classes are included. Depending on the nature of (and distance from) the emitting source and the noise realization, the visibility of the HFF can vary significantly.

3.2.2. SNR populations of samples

For a more complete landscape of the GW signals that are present in our TF image samples, Fig. 11 shows the distributions of their SNR values. These distributions are separated by classes (i.e., the CCSN emitting models) and chosen distances (1Kpc, 5Kpc, and 10 Kpc), considering the three

interferometric noise data.

At this point, it is important to identify the main trends in the SNR histograms shown in Fig. 11. As a statistical description of the input data, they have important clues to interpret, to some extent, the ResNet50 predictions.

Regarding the sample count in terms of SNR values, we can see that the greater the distance, their occurrence tends to be displaced at lower SNR values than those at shorter distances. This behavior is consistent with what we observed in Fig. 10, namely that at greater distances, for the Morozova model and more for the Andresen model, visibility of the HFF decreases, which, in other words, means that noise realization dominates over the appearing of those GW signals. The TF image samples shown in the mentioned figure are representative because, through a random exploration of dozens of samples, we found that samples with a lower (or even null) visibility of the HFF are more common among those generated at larger distances, both for the Morozova model and even more for the Andresen model. The case of the Cerdá-Durán GW signal is different because, even though we observe the same statistical behavior of low SNR values at greater distances (5Kpc and 10 Kpc), the HFF is still visible. After all, the magnitude of the GW signal is large enough to be unaffected by the magnitude of the noise.

Another trend has to do with the overlapping of SNR distributions for different distances, considering a specific model injected into specific interferometric noise data (either L1, H1, or V1). Here we observe that, as the GW model has a smaller magnitude strain and/or the noise has a smaller sensitivity, histograms at larger distances (5Kpc and 10Kpc) tend to be very overlapped, indeed, in a region of lower SNR values. From an astrophysical point of view, this behavior comes from the fact that a GW strain scales as $10/\text{distance}$, giving a really small variation at larger distances. This overlapping trend is really clear with the Andresen model (which has the smallest magnitude strain, as shown in Fig. 3) being injected into the noise data of the three detectors and the Morozova model being injected into the V1 noise data (which in turn has the smaller sensitivity, as it is shown in Fig. 1). The SNR distribution at 1Kpc has little to no overlap with the SNR distributions for the other two distances. We also notice that all SNR distributions associated with the Cerdá-Durán GW model, i.e., for all chosen distances and interferometric noises, have a little overlap with each other.

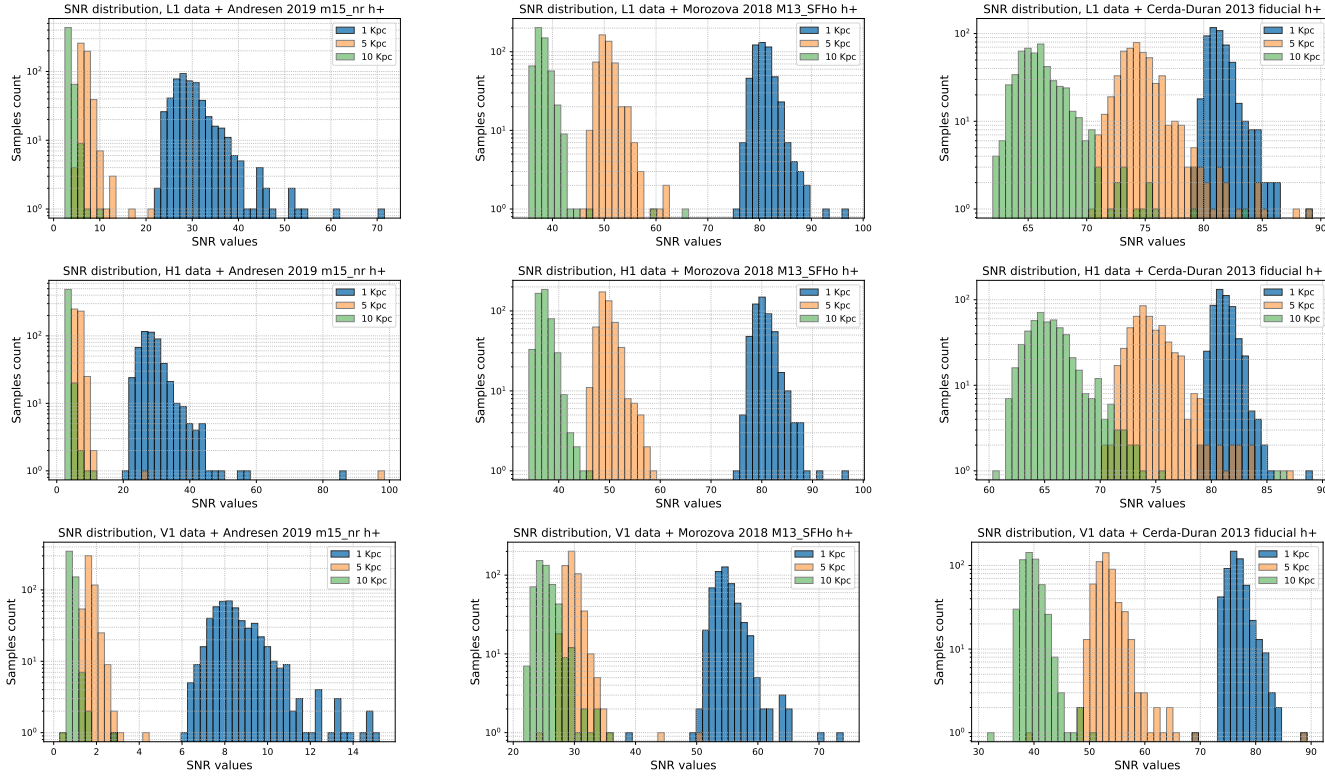


Figure 11: SNR distributions of TF image samples containing interferometric noise plus general relativistic CCSN GW models. Here, we identify three trends. Firstly, the greater the distance, the greater the occurrence of samples with lower SNR values than those at smaller distances. Besides, for a specific CCSN GW model and specific noise data, SNR histograms at larger distances tend to be more overlapped in a region of low SNR values. Finally, for a single CCSN GW model, we have that the relative dispersion of SNR distributions at different distances does not vary significantly with respect to the background noise.

Finally, let us focus on the relative dispersion of the distributions at different distances, which seem to be unique to the model and common to the three noise data. If we consider the three left plots in Fig. 11 for samples with the Andresen GW model, we can see that at 1Kpc the SNR distribution is approximately 3 times more dispersed than distributions at 5Kpc and 10Kpc. This is not the case for the Morozova GW model and the Cerdá-Durán GW model, in which their SNR distributions, for all distances, have similar dispersions (of just over a dozen SNR units). Therefore, the third trend is that the relative dispersion of the SNR distributions of a model at different distances does not vary with respect to the interferometric noise.

We stress that, after fixing the distance and the noise data, a SNR distribution is unique to its particular CCSN GW model. Therefore, differences between SNR distributions for different models imply that recognizing samples of one class can be easier (or more difficult) than others. As will be shown in the next section, this aspect is more evident when working with larger distances.

3.2.3. Testing the optimized ResNet50 model

Now we present results obtained from testing our optimized ResNet50 model, working with samples containing noise plus general relativistic CCSN GW signals. Table 5 shows test accuracies and test losses for different noise data and distances from the source. These clearly show that, independent of the noise, the performance of the model decreases as we increase the distance. Moreover, comparing results by noise data, we find that the best performances are obtained using L1 and the worst performances using V1. Given the sensitivity of detectors (shown in Fig. 1) and SNR values of the dataset (shown in bottom plots of Fig. 11), it is expected that the lowest performances occur with V1 noise data. However, it would have to be explained why at 5Kpc and 10Kpc, test accuracy drastically decreases by about 30%, pointing out that predictions for one of the three classes are, for the most part, incorrect.

To better understand the results of Table 5 (particularly to elucidate the ability of ResNet50 to recognize the HFF depending on the sample class), we present in Fig. 12 confusion matrices for all the tests performed. Here we adopt a convention in which the sum of all elements is 100%; therefore, an ideal classification gives a diagonal matrix with 33% elements.

According to the confusion matrices, in most cases (L1 and H1 at 1Kpc and 5Kpc, and V1 at 1Kpc) we have that class 1 samples (Andresen GW

Noise data	Distance (Kpc)	Test accuracy	Test loss
L1	1	0.9867	0.04617
	5	0.9333	0.4856
	10	0.8533	0.8829
H1	1	0.9767	0.08379
	5	0.8933	0.6116
	10	0.8000	1.413
V1	1	0.9133	0.5717
	5	0.6433	3.235
	10	0.5933	3.189

Table 5: Evaluation metrics for the tests performed with the optimized ResNet50 model and samples containing general relativistic CCSN waveforms. Independent of the noise, performance decreases as we increase the distance from the CCSN. The best performances are achieved using L1 data, and the worst performances are achieved using V1 data.

model) are the most difficult to recognize, with a classification percentage varying from 22.67% to 32.00%. These are followed by class 2 samples (Morozova GW model) and class 3 samples (Cerdá-Durán GW models), which are fully recognized in 33.33% of the predictions per class.

At this point, it is useful to remember what was pointed out in works [26, 20], namely that any detection machine learning algorithm not only inputs image samples as single templates (as is the case with Matched Filter) but also the distribution of these samples, that is to say, all the information about the dataset. Because of this, we can take advantage of the fact that the SNR populations of our input datasets give us valuable statistical information to understand, to some extent, the predictions of the ResNet50 algorithm. Therefore, under this framework, we can indeed observe that previously shown performance results are consistent with SNR populations of Fig. 11: In all these cases, we have that the SNR distributions for samples with the Andresen model, being located in ranges of lower SNR than those of samples with the Morozova and the Cerdá-Durán models, are spaced enough to have almost zero overlap with the SNR distributions of those other models.

On the other hand, tests performed with L1 and H1 noise data at 10Kpc show a slightly different trend. Here, the class 2 samples (Morozova) are the most misclassified, followed by the class 1 samples (Andresen), with a percentage discrepancy of 2% to 3.33% (Cerdá-Durán samples maintain the full correct classifications of 33.33%). If we again contrast these results with

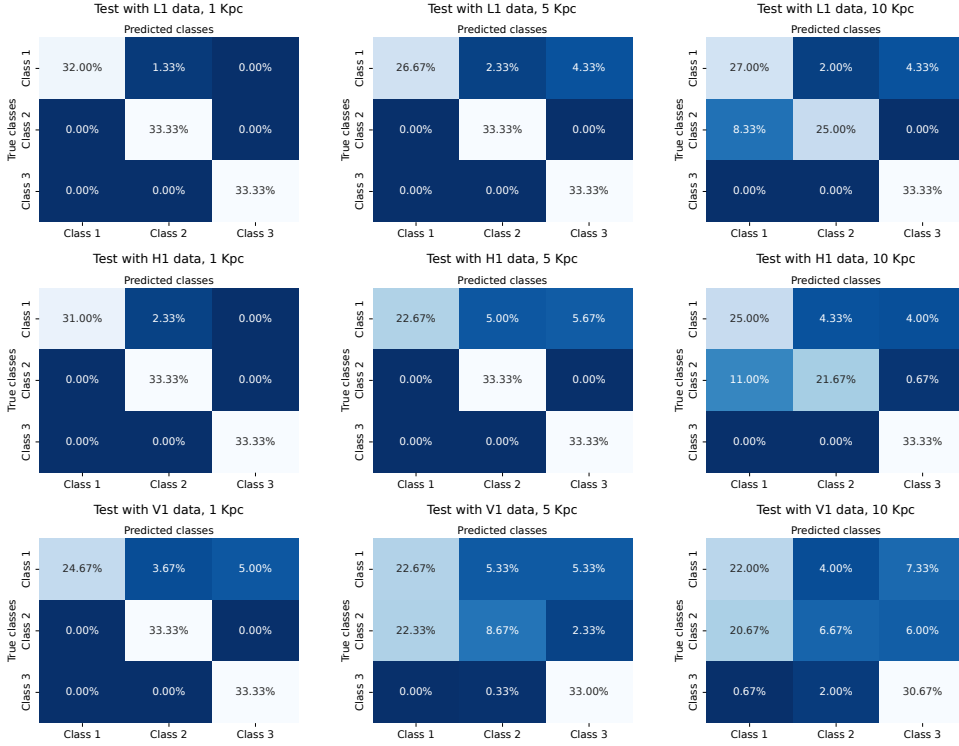


Figure 12: Confusion matrices obtained from applying the optimized ResNet50 algorithm to classify the HFF in TF image samples containing single-interferometric noise plus general relativistic CCSN GW signals. To appropriately understand these results, it is crucial to analyze the nature of our input data, which is mainly codified in the SNR distributions of the training and testing datasets (shown in Figs. 5 and 11, respectively).

the SNR populations in Fig. 11, they would seem counter-intuitive; the SNR distributions for the Andresen and Morozova models, at 10Kpc with the L1 and H1 data, are still spaced enough with zero overlapping. That is to say, in this situation, the SNR values with Andresen models slightly surpass 10, and SNR values with Morozova models are not lower than 35, approximately.

To explain the above predictive behavior of ResNet50, we need to consider not only the nature of the test dataset, but also the nature of the dataset with which we trained the algorithm, that is, the dataset of image samples containing L1, H1, and V1 data noise plus phenomenological waveforms. If we remember the histogram shown in the right panel of Fig. 5, we see that the SNR distribution for class 2 samples begins approximately at SNR= 25. This means that if in a test we input class 2 samples of SNR very close (or lower) to

the aforementioned critical value, it will be more difficult for the ResNet50 to correctly classify them because the learning was based on a reduced number of train exemplars. This difficulty is more about the insufficiency of learning samples (to correctly associate common characteristics present in training samples and test samples) than working with lower SNR values.

The above explanation becomes even clearer if we focus on the most extreme and interesting failure cases, namely tests with V1 data at 5Kpc and 10Kpc. In these tests, we have a curious result: most of the class 2 samples are predicted as class 1 samples: at 5Kpc, 23.33% of the class 2 test data were misclassified as class 1, and at 10Kpc, 20.67% of class 2 test data were misclassified as class 1. These results can be interpreted by two interrelated facts as follows: Firstly, testing with V1 data at 5Kpc and 10Kpc implies that we are working with the lowest SNR values, as shown in the bottom panel of Fig. 11, and this decreases the visibility of the HFF slope as we observed in samples of Fig. 10. Under this setting, it is expected that in a significant number of class 1 and class 2 samples, the magnitude of background noise is dominant over the magnitude of the GW strain, and the ResNet50 algorithm has to take a decision about these, even if wrong. Then, this fact explains why most of the 33.33% images of class 2 were wrongly predicted. But now the question about why these samples were misclassified as class 1 (and not as class 3) arises, and the answer brings us to the second fact, which has to do, again, with the nature of the training set, which we explain below.

Regarding the right panel of Fig. 5, we mentioned that the SNR distribution of the training class 1 samples is shifted to lower SNR values than those of the SNR distributions of class 2 and 3 samples. In fact, according to the histograms, we have that approx. at $\text{SNR} < 25$ the ResNet50 algorithm was trained only with class 1 samples; even in the region $25 < \text{SNR} < 35$, the number of class 1 samples is considerably larger than the class 2 and class 3 samples (more than 300 samples vs. a hundred samples combining class 2 and 3). Therefore, when we input class 2 image samples of $\text{SNR} < 35$ in the test (which is the case working with V1 data at 5Kpc and 10Kpc, as it is shown in the bottom panel of Fig. 11), the ResNet50 favors class 1 predictions because it was trained mostly with those samples in this low SNR regime. Like tests with L1 and H1 data at 10Kpc, the training dataset did not provide enough information for the ResNet50 to correctly recognize the HFF slope in class 2 samples in this SNR regime, and it takes a decision based on what it knows.

Results shown in confusion matrices suggest that, undoubtedly, in the

low SNR regime, the viability of our methodology is affected. However, this is not due to a malfunction of the ResNet50 architecture itself; this, as a standard computer vision model, is still very powerful (to the point that in the low SNR regime, it knew how to make what was the best decision *given the training dataset*). But rather, the quality of our training dataset in this regime is not the best to ensure an appropriate classification. Therefore, here we stress that taking into account the SNR distributions of input (training and test) datasets is truly crucial for interpreting the predictive behavior of the optimized ResNet50 algorithm. And, more important is that by generating a high-quality dataset in terms of their SNR values (i.e., broad distributions that properly inform the learning process in all SNR regimes), we will have better conditions to perform predictions. The implementation of a systematic methodology to improve input image samples in terms of their SNR values is a relevant topic for future work.

4. Conclusions

In this work, we present the first application of an optimized ResNet50 model (one of the state-of-the-art architectures in computer vision) to classify the HFF present in Morlet wavelet scalograms, i.e., TF image samples, of CCSN GW signals embedded in real interferometric noise. This task is highly relevant to advance the understanding of the detectability of the HFF. We found that this detectability varies considerably depending on the nature of (and distance from) the emitting CCSN model, the noise realization, and the input datasets given the distribution-learning property of the ResNet50 algorithm.

We show that our optimized ResNet50 algorithm can recognize the HFF by inputting TF image samples containing interferometric noise plus phenomenological and general relativistic CCSN GW signals. Using samples with general relativistic CCSN GW signals, test accuracies vary in consistency with the nature of the input datasets. Main aspect of this nature is codified the SNR distributions. Then, it was possible to interpret the predictions by analyzing these distributions.

We optimized the ResNet50 using TF image samples combining noise data from all LIGO-Virgo detectors (L1, H1, and V1) plus phenomenological waveforms. For the hyperparameter tuning, we used a `GridSearchCV` methodology and we found that the best hyperparameter combination is: batch size $b_s = 75$, number of training epochs $n_e = 40$, learning rate $\alpha = 0.01$,

momentum $m = 0.6$, and optimizer RMSprop. Then, we trained the model with the best hyperparameter combination, and, after the testing, we reached excellent results: an accuracy of 0.994178 and a (categorical cross-entropy) loss of 0.0303579.

Then, we applied a test using image samples containing noise plus general relativistic waveforms obtained from CCSN multidimensional simulations. These waveforms are more relevant for astrophysical purposes. Here, the performance varied depending on the distance from (and nature of the) CCSN emitting source and the input datasets. With L1 and H1 data at 1Kpc and 5Kpc, and with V1 data at 1Kpc we reach excellent results. Image samples containing the Morozova model (class 2) and the Cerdá-Durán model (class 3) are fully detected, 33% of the test dataset per class; and an important percentage of samples containing the Andresen model (class 1) were recognized, from 22.67% to 32.00% of the test dataset. In this setting, the viability of our methodology is clearly shown.

On the other hand, working at 10Kpc using L1 and H1 data and, more evidently, at 5Kpc and 10Kpc using V1 data, the situation is different. With L1 and H1 data, the ability to recognize image samples was adversely affected, even though results still show good statistical performance. With the Morozova model, 25% and 21.67% of the test dataset were detected, respectively; and with the Andresen model, 27% and 25% of the test dataset were detected, respectively. However, the setting of V1 data and the furthest distances is unviable for the HFF recognition with the Morozova model (and also for the Andresen model, as detailed below), because most of the samples containing this model were misclassified as Andresen samples: 22.33% and 20.67% of the test dataset were detected, for 5Kpc and 10Kpc, respectively. Samples containing the Cerdá-Durán model, even in these last configurations, are recognized enough by the ResNet50 algorithm: 33% for 5Kpc and 30.67% for 10Kpc, which is still excellent.

We were able to interpret the above undesirable misclassifications, especially in the most extreme cases of V1 data at 5Kpc and 10Kpc with Morozova and Andresen models. They have to do with the nature of the input datasets, both in the training (samples with noise plus phenomenological waveforms) and the testing (samples with noise plus general relativistic CCSN waveforms). This nature is mainly codified in their SNR distributions. By observing these distributions, we found that in the low SNR regime, the ResNet50 algorithm was trained with an insufficient amount of data: a few samples with the Andresen model and no samples with the Morozova model.

This, complemented by the fact that the noise realization dominates over the GW signals (i.e., the visibility of the HFF is lost) in a high percentage of Andresen and Morozoca samples, explains why most samples with the Morozova model are mostly misclassified as samples with the Andresen model. Therefore, in this setting, our methodology is unviable.

Our classification strategy to characterize the HFF directly impacts the parameter estimation research program with CCSN GW signals because it is aimed not only to predict the dynamical behavior of the HFF but also to explain its occurrence in observational samples depending on several factors such as the nature of (and the distance from) the CCSN model and the noise realization. In addition, our methodology is general enough because it does not assume anything about the continuity and/or discontinuity of HFF slope values, which is a matter of ongoing theoretical research.

Using only single-interferometer data in our study really shows the strength of our methodology and results, because we will give minimal information to the ResNet50 to learn (only one TF image sample per detection), and still we reach excellent results. Anyway, our implementation can be easily adapted to a complete process of CCSN GW signals detection in a network of three detectors and HFF characterization. In that case, we would only need to input simultaneous TF image samples along the three RGB channels without any modification in the architecture of the ResNet50, reducing the HFF characterization to a simple transfer learning procedure.

Now, apart of the above advantages, our methodology has also limitations, particularly related to predictions in low SNR regime. In that sense, we also conclude that the ResNet50 classification model will be more or less viable, depending on the particular configuration that we have: GW CCSNe model, noise realization, and input (training and testing) datasets, given the learning-distribution property of the ResNet50 algorithm. In particular, how to improve the quality of the input datasets to reach good performance results with further distances and larger noise realizations is an aspect that deserves to be addressed in future works. Other relevant aspects as the source orientation, and the inclusion of data from a network of more than three detectors is also a matter that would need to be addressed in prospective research.

Acknowledgement

This work was supported by CONAHCYT Frontiers Science project No. 376127 *Sombras, lentes y ondas gravitatorias generadas por objetos compactos*

astrofísicos. M.D.M. acknowledge the support of CONAHCYT postdoctoral project No. 3751010, CONAHCYT Frontiers Science project No. 376127, and PROSNI-UDG. C.M. wants to thank CONAHCYT and PROSNI-UDG. This research has used data or software obtained from the Gravitational Wave Open Science Center (gwosc.org), a service of the LIGO Scientific Collaboration, the Virgo Collaboration, and KAGRA. This material is based upon work supported by NSF's LIGO Laboratory which is a major facility fully funded by the National Science Foundation, as well as the Science and Technology Facilities Council (STFC) of the United Kingdom, the Max-Planck-Society (MPS), and the State of Niedersachsen/Germany for support of the construction of Advanced LIGO and construction and operation of the GEO600 detector. Additional support for Advanced LIGO was provided by the Australian Research Council. Virgo is funded, through the European Gravitational Observatory (EGO), by the French Centre National de Recherche Scientifique (CNRS), the Italian Istituto Nazionale di Fisica Nucleare (INFN) and the Dutch Nikhef, with contributions by institutions from Belgium, Germany, Greece, Hungary, Ireland, Japan, Monaco, Poland, Portugal, Spain. KAGRA is supported by Ministry of Education, Culture, Sports, Science and Technology (MEXT), Japan Society for the Promotion of Science (JSPS) in Japan; National Research Foundation (NRF) and Ministry of Science and ICT (MSIT) in Korea; Academia Sinica (AS) and the National Science and Technology Council (NSTC) in Taiwan.

References

- [1] B. Abbott, R. Abbott, T. Abbott, M. Abernathy, F. Acernese, K. Ackley, et al., Observation of Gravitational Waves from a Binary Black Hole Mergers, *Phys. Rev. Lett.* 116 (2016) 061102.
- [2] B. Abbott, R. Abbott, T. Abbott, F. Acernese, K. Ackley, C. Adams, et al., GW170817: Observation of Gravitational Waves from a Binary Neutron Star Inspiral, *Phys. Rev. Lett.* 119 (2017) 161101.
- [3] B. Abbott, R. Abbott, T. Abbott, F. Acernese, K. Ackley, C. Adams, et al., Gravitational Waves and Gamma-Rays from a Binary Neutron Star Merger: GW170817 and GRB 170817A, *ApJL* 848 (2017) 2.
- [4] M. Szczepańczyk, J. Antelis, M. Benjamin, M. Cavagliá, D. Gondek-Rosińska, T. Hansen, et al., Detecting and reconstructing gravitational

- waves from the next galactic core-collapse supernova in the advanced detector era, *Phys. Rev. D* 104 (2021) 102002.
- [5] K. Kotake, K. Sato, K. Takahashi, Explosion mechanism, neutrino burst and gravitational wave in core-collapse supernovae, *Rep. Prog. Phys.* 69 (2006) 971.
 - [6] E. Abdikamalov, G. Pagliaroli, D. Radice, Gravitational Waves from Core-Collapse Supernovae, in: C. Bambi, S. Katsanevas, K. Kokkotas (Eds.), *Handbook of Gravitational Wave Astronomy*, 2022.
 - [7] V. Morozova, D. Radice, A. Burrows, D. Vartanyan, The gravitational wave signal from core-collapse super-novae, *Astrophys. J.* 861 (2018) 10.
 - [8] A. Casallas-Lagos, J. Antelis, C. Moreno, M. Zanolin, A. Mezzacappa, M. J. Szczepańczyk, Characterizing the temporal evolution of the high-frequency gravitational wave emission for a core collapse supernova with laser interferometric data: A neural network approach, *Phys. Rev. D* 108 (2023) 084027.
 - [9] Z. Lin, A. Rijal, C. Lunardini, M. Morales, M. Zanolin, Characterizing a supernova’s standing accretion shock instability with neutrinos and gravitational waves, *Phys. Rev. D* 107 (2023) 083017.
 - [10] T. Bruel, M.-A. Bizouard, M. Obergaulinger, P. Maturana-Russel, A. Torres-Forné, P. Cerdá-Durán, et al., Inference of protoneutron star properties in core-collapse supernovae from a gravitational-wave detector network, *Phys. Rev. D* 107 (2023) 083029.
 - [11] K. He, X. Zhang, S. Ren, J. Sun, Deep Residual Learning for Image Recognition, *IEEE Conference on Computer Vision and Pattern Recognition (CVPR)* (2016) 770–778.
 - [12] P. Astone, P. Cerdá-Durán, I. D. Palma, M. Drago, F. Muciaccia, C. Palomba, F. Ricci, New method to observe gravitational waves emitted by core collapse supernovae, *Phys. Rev. D* 98 (2018) 122002.
 - [13] A. Mezzacappa, M. Zanolin, Gravitational Waves from Neutrino-Driven Core Collapse Supernovae: Predictions, Detection, and Parameter Estimation, *arXiv:2401.11635* (2024).

- [14] P. Welch, The use of fast Fourier transform for the estimation of power spectra: A method based on time averaging over short, modified periodograms, *IEEE Transactions on Audio and Electroacoustics* 15 (1967) 70–73.
- [15] C. E. T. Alonso, C. Moreno, M. D. Morales, M. Antelis, Detector de ondas gravitacionales fenomenológicas de supernovas basado en aprendizaje supervisado, *Research in Computing Science* 152(6) (2023) 259–271.
- [16] H. Andresen, E. Muller, H.-T. Janka, A. Summa, K. Gill, M. Zanolin, Gravitational waves from 3d core-collapse supernova models: The impact of moderate progenitor rotation, *MNRAS* 486 (2019) 2238–2253.
- [17] P. Cerdá-Durán, N. DeBrye, M. Aloy, J. Font, M. Obergaulinger, Gravitational wave signatures in black hole forming core collapse, *Astrophys. J. Lett.* 779 (2013) L18.
- [18] A. Nitz, I. Harry, D. Brown, C. Biwer, J. Willis, T. Canton, et al., gwastro/pycbc: v2.4.0 release of PyCBC (2023). doi:10.5281/zenodo.10013996.
- [19] R. Kronland-Martinet, J. Morlet, A. Grossmann, Analysis of sound patterns through wavelet transforms, *Int. J. Patt. Recogn. Art. Intell.* 1 (1987) 273–302.
- [20] M. Morales, J. Antelis, C. Moreno, A. Nesterov, Deep Learning for Gravitational-Wave Data Analysis: A Resampling White-Box Approach, *Sensors* 21(9) (2021) 3174.
- [21] A. Clark, Pillow (pil fork) (2015).
URL <https://python-pillow.org/>
- [22] M. Shafiq, Z. Gu, Deep Residual Learning for Image Recognition: A Survey, *Appl. Sci.* 12(18) (2022) 8972.
- [23] T. GoogleBrain, Tensorflow (2023). doi:10.5281/zenodo.10126399.
- [24] F. Chollet, et al., Keras (2015).
URL <https://keras.io>

- [25] R. Abdulkadirov, P. Lyakhov, N. Nagornov, Survey of Optimization Algorithms in Modern Neural Networks, *Mathematics* 11(11) (2023) 2466.
- [26] T. Gebhard, N. Kilbertus, I. Harry, B. Schölkopf, Convolutional neural networks: A magic bullet for gravitational-wave detection?, *Phys. Rev. D* 100 (2019) 063015.